Corrections of surface fissure effect on apparent resistivity measurements

Julien Gance, P. Sailhac, Jean-Philippe Malet

Geophysical Journal International

Geophys. J. Int. (2015) **200,** 1116–1133 doi: 10.1093/gji/ggu453

GJI Marine geosciences and applied geophysics

Corrections of surface fissure effect on apparent resistivity measurements

J. Gance,[1,2] P. Sailhac[1] and J.-P. Malet[1]

[1]*Institut de Physique du Globe de Strasbourg, CNRS UMR* 7516, *EOST/Université de Strasbourg,* 5 *rue René Descartes, F*-67084 *Strasbourg Cedex, France. E-mail: julien.gance@gmail.com*

[2]*BRGM, Bureau de Recherches Géologiques et Minières,* 3 *Avenue Claude Guillemin, F*-45060 *Orléans, France.*

Accepted 2014 November 18. Received 2014 September 30; in original form 2014 March 20

SUMMARY

Electrical resistivity tomography (ERT) is a useful tool to detect and track water flow paths in the subsoil. However, measurements are strongly affected by subsurface heterogeneities such as fissures of different sizes and genesis (shrinking-swelling, macropores and deformation). In this work, we focus on surface fissures characterized by dimensions lower than the interelectrode spacing and correct their effect on apparent resistivity pseudo-sections by incorporating fissure geometry in the topography. We show that fissures with depths greater than 0.10 times the interelectrode spacing for a dipole–dipole array and equal to 0.16 for the gradient array and the Wenner–Schlumberger arrays create significant anomalies (greater than 5 per cent) in the pseudo-section. Surface fissure widths and dip angles have little effect with respect to the fissure depths which can increase the apparent resistivity up to 200 per cent. The clogging of the fissures with water or soil material decreases the anomaly effect linearly with the percentage of filling. The correction of apparent resistivity values is possible for relatively simple fissure geometries and only requires a manual survey of the surface fissures. It allows to improve the quality of the inverted resistivity section by mitigating the inversion artefacts and therefore a better interpretation.

Key words: Tomography; Electrical properties; Geomorphology; Hydrogeophysics; Fracture and flow.

1 INTRODUCTION

Electrical resistivity tomography (ERT) is a hydro-geophysical technique suitable to monitor spatial and temporal variation of soil water content and to characterize water fluxes in the subsoil. It has been used in a variety of applications such as in agricultural studies to survey soil wetting and drying (Michot *et al.* 2003; Srayeddin & Doussan 2009), in geotechnical studies for estimating the stability of earth embankments (Jackson *et al.* 2002), in geological studies to identify preferential water flow paths within heterogeneous landslide deposits (Suzuki & Higashi 2001; Travelletti *et al.* 2012), in hydrogeological studies to understand the flow behaviour in karstified limestones Robert *et al.* (2012) or in environmental studies to define the circulation of leachate in waste deposits (Clément *et al.* 2011).

The technique is sensitive to small scale surface or subsurface heterogeneities such as roots (Amato *et al.* 2008), surface fissures (Samouëlian *et al.* 2003; Amidu & Dunbar 2007) or soil compaction differences (Ritz *et al.* 1999; Michot *et al.* 2003; Besson *et al.* 2004). These heterogeneities do not only modify locally the soil hydrological properties but can drastically change the hillslope hydrology (Van Asch *et al.* 1999; Krzeminska *et al.* 2011; Dinka 2012). The detection of preferential water flow paths and the quantification of the associated water fluxes are thus major issues in many environmental applications.

Although being very sensitive to those features, ERT is generally not able to image their geometry. Bobachev *et al.* (1995) and Ritz *et al.* (1999) demonstrated that the heterogeneities can distort electrical sounding curves and apparent resistivity pseudo-sections leading to possible erroneous geological interpretations. A major issue is that inversion results can be strongly affected by these heterogeneities because of the presence of inversion artefacts. This effect is rarely studied in the literature but has been illustrated by Ferahtia *et al.* (2009) in the case of strong noise spikes. For the particular case of surface fissure, few studies really deal with these problems. In order to investigate the effect of surface fissure on ERT, we first present a field experiment realized at the Super-Sauze landslide to illustrate fissure effect on ERT. Secondly, we describe the methodology used to correct the apparent resistivity pseudo-section for surface fissure effects. Third, we perform a sensitivity analysis of apparent resistivity to different descriptors of the surface fissure geometry. We finally apply the proposed correction methodology on a real data set.

2 EFFECT OF SURFACE FISSURES ON A REAL DATA SET

We realized a controlled infiltration experiment with ERT monitoring at the Super-Sauze landslide, developed in the

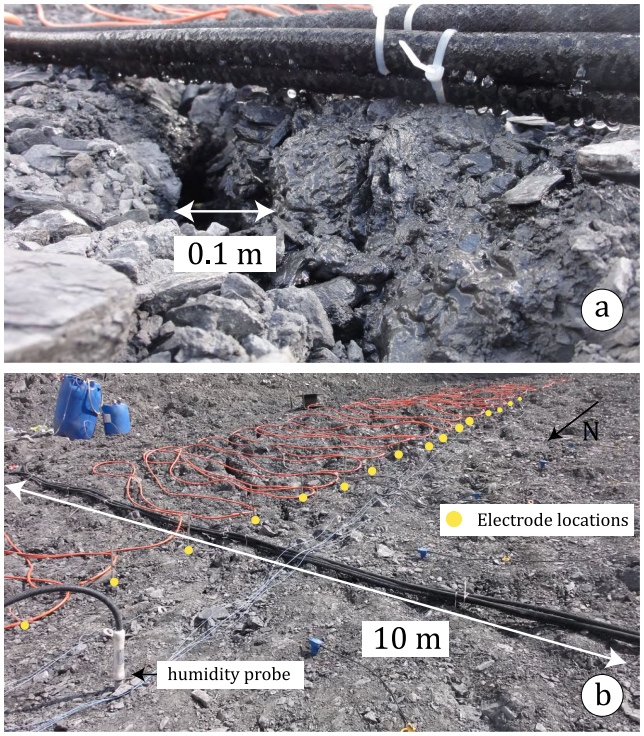

Figure 1. Controlled infiltration experiment on a fissured surface monitored by ERT: (a) drops of water at the outlet of the porous pipe and (b) global view of the infiltration experiment.

Callovo-Oxfordian black marls formation of the Barcelonnette basin (South French Alps). The soil investigated is the results of the degradation of the rock, and is thus very heterogeneous. The grain size corresponds to 25 per cent of silts and clays, 35 per cent of sand and 40 per cent of gravel (Fig. 1a). The intact soil (e.g. not fissured) has a mean resistivity of 30 Ωm in the subsurface (1–3 m). The unfissured soil has a mean resistivity of 30 Ωm in the first metres of depth. We realize this experiment on a highly fissured area located in the upper part of the landslide. The slope angle is almost constant along the investigated profile and several fissures with orientations globally perpendicular to the steepest slope direction are observed. Their strike angle is mainly perpendicular to the profile direction. Fissure density is very heterogeneous (Fig. 2) and is globally higher in the upper part of the profile (0.86 fissure per linear metre on average) than in the lower part (0.50 fissure per linear metre on average). The fissure widths range between 0.05 and 0.20 m. Their depths range between 0.05 and 0.70 m and are larger in the lower part of the profile than in the upper part. Fissures are almost parallel to each other, except in the lower part of the profile where fissure intersect with complex geometries.

The experiment has been designed to be as much as possible close to the 2-D assumption. It consists in slowly infiltrating water along a percolation line using porous pipes (Fig. 1a). This technique allows avoiding surface run-off. The water flow in the subsoil is tracked using time-lapse ERT. A Syscal Pro resistivimeter is used to measure resistivity along a 2-D profile constituted of 60 electrodes, regularly spaced of 0.50 m, stuck into the ground at a depth of 0.1 m. We used a dipole–dipole (DD) and a Wenner–Schlumberger (WS) configurations fully described in Appendix A. The quality of the measurements is assessed by computing the standard deviation of the five measurements performed for each quadrupoles. Measurements with standard deviation higher than 7 per cent have been removed.

The apparent resistivity pseudo-section acquired before the infiltration is presented in Fig. 2(c). A classic inversion (i.e. using the L_2 norm and default settings) of this data set performed with the code of Günther *et al.* (2006) is presented in Fig. 2(b) with a colour

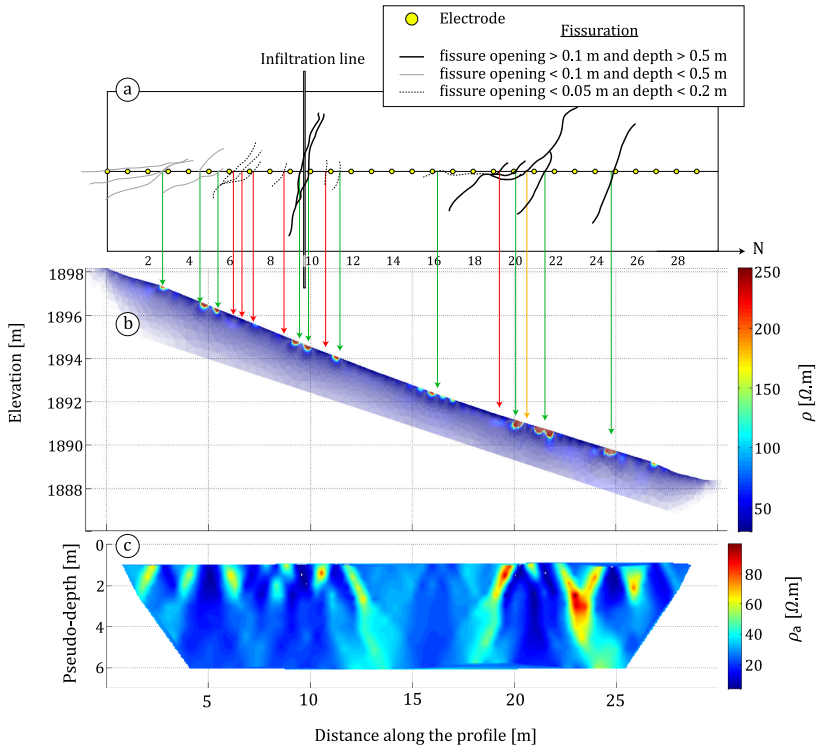

Figure 2. Effect of surface fissures on a real data set at the Super-Sauze landslide acquired with a dipole–dipole configuration (detailed in Table A1): (a) map of surface fissures; (b) inverted resistivity and (c) pseudo-section of apparent resistivity used for the inversion.

scale chosen to highlight the fissure anomalies ranging between 5 and 250 Ωm. The inversion rms error equals to 4.75 per cent with a χ^2 value of 1.9 and the maximal resistivity in the model equals to 5760 Ωm.

The result confirms the sensitivity of ERT to fissures. In the apparent resistivity pseudo-section, 'pants-leg' patterns are visible, as observed for shallow cavities on DD array pseudo-sections (Jung & Park 2005), with values ranging from 5 to 100 Ωm within a slope characterized by a mean apparent resistivity approximately equal to 30 Ωm. The location of the fissures is not directly visible in the raw data set. However, in the inverted resistivity section, several resistive anomalies at the surface are visible. Fissures larger than 0.05 m and deeper than 0.20 m result in large anomalies ($\geq$250 Ωm) after inversion. Smaller fissures also cause anomalies ($\leq$100 Ωm), less visible with this colour scale.

The geometry of the anomalies is not representative of the fissure geometry. Most of them measure 0.50 m in width (e.g. corresponding to the interelectrode spacing) and are not centred at the exact fissure position. The geometry of the anomalies is characterized by large oval shape, very different from the thin triangular elements that could be expected. Moreover, we notice that between abscissas 19 and 21 m, some fissures larger than 0.10 m and deeper than 0.50 m do not result in resistivity anomaly. This observation can be explained by the spatial connection of the fissures resulting in a larger but unique resistivity anomaly. Finally, the amplitude of the anomalies varies for all fissures, possibly depending on the fissure size. The amplitudes of the anomalies are therefore not representative of the reality, and are different from the constant and infinite air resistivity.

The anomalies visible on the pseudo-section of apparent resistivity can be explained from a qualitative point of view. Indeed, the ERT method consists in injecting a dc (or considered as) electric current (I) in the soil by two electrodes (A and B) constituting the injection dipole. Then, the electric potential (ΔV) difference is measured between two electrodes M and N constituting the measurement dipole. The soil resistance R computed as $\Delta V/I$ depends on the ABMN quadripole geometry. Resistances measured with different quadripole geometries cannot be compared. To overcome this problem, the soil apparent resistivity parameter ρ_{app} (Ωm), is used and is calculated as follows:

$$\rho_{\text{app}} = k\frac{\Delta V}{I}, \tag{1}$$

where I is the injected current (A), ΔV is the electrical potential difference (V) and k is the geometrical factor (m). Usually, the geometrical factor k is computed under the hypothesis of a flat semi-infinite homogeneous half-space according to eq. (2) that determines the soil apparent resistivity for any quadripole located at the surface (Scollar *et al.* 1990).

$$k_{\text{usual}} = 2\pi\left[\frac{1}{\frac{1}{AM}-\frac{1}{BM}-\frac{1}{AN}+\frac{1}{BN}}\right]. \tag{2}$$

The calculated soil apparent resistivity corresponds to the true soil resistivity in the particular case of a homogeneous half-space with a flat topography. However, in practice, the measurements are always affected by the topography and the possible presence of surface fissures, leading to anomalies in the pseudo-section (Tsourlos *et al.* 1999; Samouëlian *et al.* 2003). Because of the non-uniqueness of the solution of the inversion and of the possible low sensitivity of ERT around fissures, anomalies in the pseudo-section are amplified in the inverted section. Therefore corrections are necessary in the preprocessing.

To the best of our knowledge, correction of the effects of surface fissure on ERT has never been applied. A study aiming at monitoring soil water content variations in a fissured soil has been conducted by Michot *et al.* (2003). However, the fissure effect is not visible in the data set because of the small size of the fissures compared to the interelectrode spacing. At smaller scale, a few studies have focused on water flow monitoring around fissures. Most of them were conducted with the aim of characterizing the geometry of the fissures (e.g. distribution, location, orientation, width and depth, Tabbagh *et al.* 2007; Sentenac & Zielinski 2009; Greve *et al.* 2010; Jones *et al.* 2012) but did not investigate the possible associated inversion artefacts. Although the use of electrical anisotropy allows avoiding the inversion step (Samouelian *et al.* 2004) and gives access to qualitative information on water flows (Greve *et al.* 2012), water content estimation from ERT data set requires to adapt the processing. The use of blocky inversion instead of least-square inversion (Jones *et al.* 2012) or specific regularization, such as flatness ratio changes during the inversion (Loke & Barker 1996), can improve the characterization of the fissures. Nevertheless, some authors believe that the inverse problem was not adapted to recover such heterogeneities, and therefore focus on the correction of apparent resistivity pseudo-sections. For shallow heterogeneities, they show the potential to correct successfully their effects by filtering the apparent resistivity pseudo-sections (Bobachev *et al.* 1995; Ritz *et al.* 1999). These filtering methods, based on pseudo-section smoothing, are not adapted for certain large resistivity anomalies (such as described previously) and have the disadvantage of not preserving the resistivity around the anomaly.

In this context, the objective of our work is to provide a new method to correct the effect of surface fissures on apparent resistivity data set to reduce artefacts in data inversion. This requires reconsidering the usual method of calculating apparent resistivity. In this work, we use the geometry of surface fissure obtained from a geomorphological survey (Fig. 2a) to take into account the fissure effects in the apparent resistivity pseudo-sections. This was not possible because forward dc modelling codes adapted to arbitrary topography were not available (Loke & Barker 1996; Loke 2000). The correction is based on the computation of the geometrical factor on a realistic model containing the fissure geometry in the profile topography. The manuscript details successively (1) the methodology used to assess ERT sensitivity to surface fissure, (2) the results of the sensitivity analysis and (3) the correction of fissure effects on a real data set and the assessment of the improvement for static and time-lapse inversions.

3 METHODOLOGY

3.1 Computation of the topographic effect

To correct the effect of fissure in the pseudo-section, we define the 'true' geometrical factor k_{true} as the geometrical factor computed for a model with an arbitrary topography (e.g. containing fissures). Its definition is identical to the definition of k_{usual}, namely, the soil apparent resistivity calculated with k_{true} is equal to the soil resistivity in the particular case of a homogeneous soil resistivity. In both cases, the apparent resistivity is defined by eq. (1) using k_{usual} or k_{true}. The effect of the topography geometry on apparent resistivity pseudo-section can therefore be summarized using the dimensionless parameter t (Rücker *et al.* 2006) defined as:

$$t = \frac{\rho_{\text{app usual}}}{\rho_{\text{app true}}} = \frac{k_{\text{usual}}}{k_{\text{true}}}, \tag{3}$$

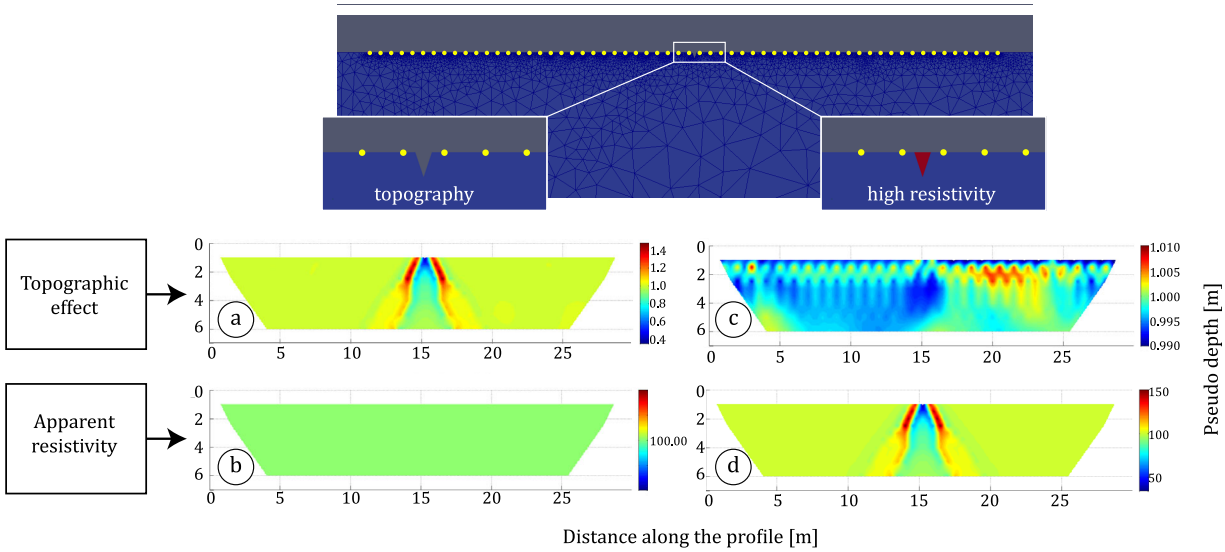

Figure 3. Differences between the topographical and the high resistivity anomaly modelling of fissures. Example for a dipole–dipole array on a semi-infinite homogeneous half-space of 100 Ωm media. The topographic effect is represented on subset (a) and (c), and the apparent resistivity on subset (b) and (d). The fissure, centred at the position 15.25 m, is vertical and its size is 0.30 m in depth and 0.20 m in width.

where t is the topographic effect, $\rho_{\text{app usual}}$ is the apparent resistivity calculated using k_{usual} and $\rho_{\text{app true}}$ is the apparent resistivity calculated using k_{true}. With a value of $t = 1$, the measurement is not affected by topography. Values of $t > 1$ refer to increased apparent resistivity whereas values of $t < 1$ indicate decreased apparent resistivity due to the topography geometry.

In case of a non-trivial topography k_{true} is unknown and can only be estimated numerically using an appropriate dc forward modelling code. In the next section, we describe the numerical code and the strategy used to model apparent resistivity.

3.2 Dc forward modelling code

The complex geometry of the topography requires the use of a flexible, accurate and quick solver of the forward dc resistivity problem. In this context, the 3-D dc resistivity modeler of Rücker *et al.* (2006) is used. It allows computing the electrical potential created by a punctual source, using the finite-element method (FEM) on unstructured tetrahedral mesh with possible local refinement of the topography. This local refinement allows maintaining an acceptable accuracy while limiting the number of nodes in the mesh. This solution appears to be particularly adapted to our problem because it is composed of a flexible mesh generator and it integrates quadratic shape functions that improve strongly the accuracy. The error estimated on a conductive half-sphere shows a relative deviation between numerical and analytical solution lower than 0.1 per cent (Rücker *et al.* 2006). Moreover, the FEM allows an perfect modelling of the topography by considering the current flow through the boundary strictly equal to zero in its formulation.

We then compute the primary potential of a model containing surface fissures by assigning a resistivity value of 1 Ωm for all the cells of the mesh. Because the media is characterized by a homogeneous resistivity, the apparent resistivity calculated is also equal to 1 Ωm. Then, the resistance calculated (ratio $\Delta V/I$) equals the inverse of the geometrical factors (see eq. 1 with $\rho_{\text{app}} = 1$ Ωm).

3.3 Differences between the classical and the proposed modelling approach

The difference between the classical method of apparent resistivity calculation and our method is the fissure modelling. On the one hand, when using k_{usual}, we implicitly consider that there is no local perturbation of the topography geometry, so that the ground is flat. If surface fissures are present, they are considered as a part of the soil and represented by a resistive soil element. On the other hand, by using k_{true}, we consider that the topography is not flat but affected by local topographical perturbations due to the presence of fissures. If surface fissures are present, they do not form part of the media and are therefore not represented as a resistive anomaly in the measurements.

Fig. 3 presents the differences between the geometrical factors and the apparent resistivity computations. In the case of a semi-infinite homogeneous model with a fissure represented by a resistive element, the topography is flat. Therefore, the geometrical factor k_{true} is equal to k_{usual}, so that the topographic effect t is equal to 1 (±1 per cent) all over the pseudo-section (Fig. 3c). The effect of fissures is therefore only visible in the apparent resistivity (Fig. 3d). In the proposed method of resistivity calculation, the geometrical factor k_{true} is computed numerically by giving a homogeneous resistivity of 1 Ωm to the model that includes the fissure in the topography. The effect of fissures is only visible in the topographic effect t (Fig. 3a) but does not appear in the apparent resistivity which is homogeneous and equal to the resistivity of the media (100 Ωm, Fig. 3b).

3.4 Design of the fissure model

To design the numerical sensitivity analysis, we define (1) relevant fissure descriptors and (2) a reference fissure with a particular size and geometry.

Fissures are generally conceptually represented by discrete elements (Rots & Blaauwendraad 1989), approximated by a thin rectangular shaped feature (Lataste *et al.* 2003; Tabbagh *et al.* 2007)

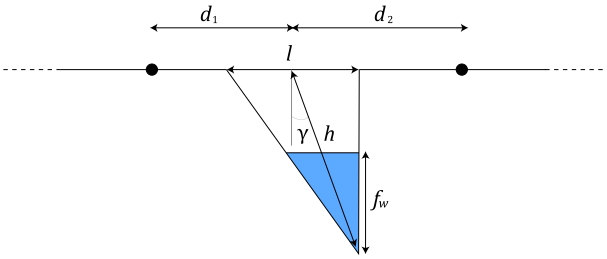

Figure 4. Fissure model used in this study with six different descriptors: depth (h), dip angle (γ), distance from the nearest electrodes (d_1 and $d2$), width (l) and water filling (f_w).

or by triangular elements (Stumpf *et al.* 2013). Fissure descriptors are various and depend on the application domain. For example, intersection, number of segments, fractal dimension and geometry of the network are used to characterize desiccation fissures (Velde 1999). Other descriptors such as position, length, width, depth and orientation are used for characterizing shrinking-swelling fissures (Tabbagh *et al.* 2007; Dinka 2012) and are more adapted to landslide fissure (Stumpf *et al.* 2013).

Among the studies aiming at characterizing the landslide fissure characteristics (Gance *et al.* 2012; Grandjean *et al.* 2012; Niethammer *et al.* 2012; Stumpf *et al.* 2013), only field surveys can provide a complete set of geomorphological descriptors (depth, width and filling). A study conducted in 2008 indicates that more than 50 per cent of the fissure widths and depths are, respectively, lower than 0.2 and 0.5 m (Espinosa 2009). Maximal fissure width and depth in the order of, respectively, 0.5 and 1.0 m. Those results come from punctual data and also depend on the survey date, but the order of magnitudes found are confirmed by another survey realized in 2011 on a restricted area (Gance *et al.* 2012), with a majority of fissures characterized by depth and width, respectively, lower than 0.2 and 0.3 m.

Based on these results, we design a 2-D profile including a fissure typical of the types observed at Super-Sauze (Fig. 4). The fissure is characterized by a depth h, a width l measured between the two edges of the fissure at the topographic surface and a dip angle γ measured as the angle between the vertical and the line joining the fissure centre and the deeper point of the fissure. The fissure is not necessarily located in the middle of a dipole. The distance from its centre to the nearest electrodes are, respectively, d_1 and d_2. The fissure can be partially filled by water (e.g. water height f_w expressed in percentage of the depth). These six descriptors are used for the sensitivity analysis. The electrode spacing is fixed at 0.50 m, which can be considered as the minimal inter electrode spacing adapted to subsurface water flow monitoring and verifying point source assumption for usual electrodes. For the experiments, the changes in descriptor values are chosen according to the field observations (Table 1). The model is built on a flat topography and

Table 1. Range of parameter used in the numerical experiments with a constant interelectrode spacing of 0.50 m.

Parameter	Variation range	Unit
d_1	0.05–0.25	(m)
d_2	0.25–0.45	(m)
l	0.01–0.40	(m)
h	0.01–1.00	(m)
γ	0–50	(°)
f_w	0–90 per cent	(per cent)

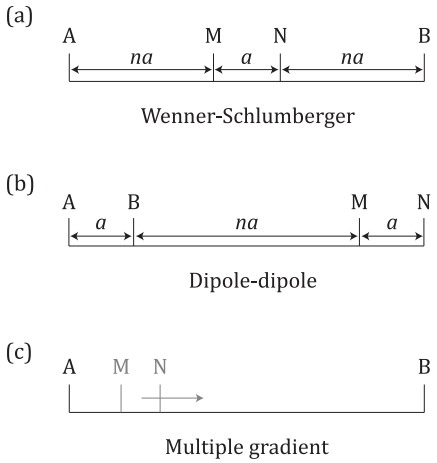

Figure 5. Schemes of the different resistivity arrays used in this study: (a) Wenner–Schlumberger; (b) Dipole–dipole; (c) multiple gradient. A and B are the current electrodes and M and N the potential measurement electrodes.

2-D invariance which is realistic with regards to the fissure sizes measured in the field (several metre on average).

To investigate the sensitivity of the different acquisition arrays, we define a reference fissure with mean descriptor values: d_1 and d_2 are both equal to 0.25 m, so that the reference fissure is centred between two electrodes. The reference width and depth, named respectively, l_0 and h_0, are equal to respectively, 0.20 and 0.30 m. The dip angle γ and the water height in the fissure are considered equal to zero, so that the reference fissure is vertical and dry.

The results obtained in the next sections are generic and can be used for any survey with equivalent scales. To facilitate the comparison between different interelectrode spacings, we define the fissure to dipole sizes ratio α and the fissure aspect ratio β such as:

$$\begin{cases} \alpha = h_0/(d_1 + d_2) \\ \beta = h_0/l_0 \end{cases} \quad (4)$$

α is larger when the fissure depth is large compared to the dipole length and β is larger when fissure depth is large compared to fissure width.

4 SENSITIVITY ANALYSIS OF APPARENT RESISTIVITY TO SURFACE FISSURE

4.1 Topographic effect for classical configurations

We first illustrate the effect of the acquisition method (resistivity arrays) on the estimation of the apparent resistivity around a fissure. Three resistivity arrays are chosen: (a) the WS array, (b) the DD array (DD) and (c) the multiple gradient array (GRAD), with quadripoles described in Fig. 5. A section of 60 electrodes with a constant 0.50 m spacing is used. A complete definition of each array can be found in Appendix A.

Apparent resistivity values are represented in pseudo-sections. Abscissa and pseudo depths computation are detailed in Table 2. Multiple gradient pseudo-sections are not easy to represent. Therefore, we use the relation from Dahlin & Zhou (2006) which allows recovering a coherent anomaly pattern (i.e. non-disseminated in the pseudo-section). The multiple gradient pseudo-section is not regular, so that measurement points can be almost superimposed. Therefore, we choose to interpolate all pseudo-sections using a

Table 2. Pseudo depth and abscissa calculation.

Array	Pseudo-abscissa (x)	Pseudo-depth (z)
Wenner–Schlumberger	$(x_M + x_N)/2$	$(x_M - x_A)$
Dipole–dipole	$(x_B + x_M)/2$	$(x_M - x_B)$
Multiple gradient	$(x_M + x_N)/2$	$\min(\lvert x - x_A \rvert, \lvert x - x_B \rvert)/3$

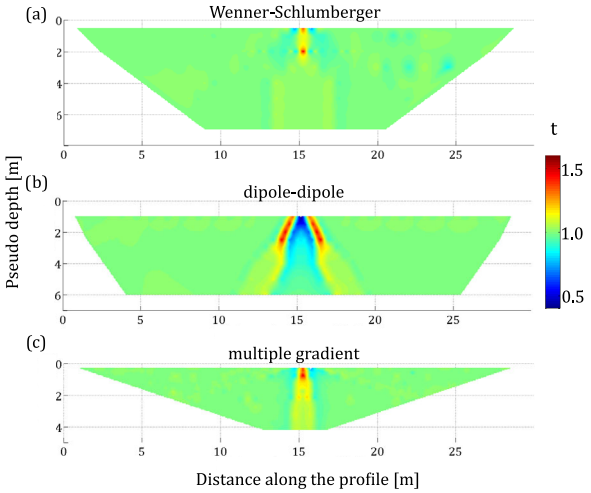

Figure 6. Pseudo-section of topographic effect (t) computed for the reference fissure and for the (a) WS, (b) DD and (c) GRAD arrays.

natural neighbour method which allow interpolating on a regular grid, keeping the original values at the measurement points (Sambridge *et al.* 1995).

Using the previously defined fissure model, modelling strategy and code, we investigate the effect of the reference fissure (h_0 equal to 0.30 m and l_0 equal to 0.20 m, α equal to 0.6 and β equal to 1.5) for these different resistivity arrays. The response is presented as a pseudo-section of topographic effect (eq. 3, Fig. 6). The result indicates that all arrays generate high and low anomalies which could be incorrectly interpreted either as the result of conductive or resistive bodies, as a poor coupling between the soil and the electrode, or as an amplification of the effect of real subsurface anomalies. The topographic effect shows different patterns according to the array. The DD array produces a low resistivity anomaly at the centre of the profile below the fissure. On each side, high apparent resistivity regions are observed (Fig. 6a). This effect widens and attenuates with depth but apparent resistivity can be multiplied or divided by a factor 2 near the surface. The GRAD and WS arrays produce an opposite topographic effect of lower amplitude. These patterns are comparable to those identified by Tsourlos *et al.* (1999) who evaluates the effect of a hill and valley-type topography on different arrays.

4.2 Critical α ratio

The previous section showed the effect of fissure on the apparent resistivity computed with the k_{SIHS} geometrical factor. It suggests considering the presence of fissures in any interpretation. The objective of this section is to assess the critical size from which the fissure significantly impact the apparent resistivity pseudo-section, with regards to the interelectrode spacing. Therefore, the fissure aspect ratio β, that controls the fissure geometry is kept constant, and the fissure to dipole size ratio α, that controls the scale of the analysis is varied ranging between 0.05 and 0.25. The variation of

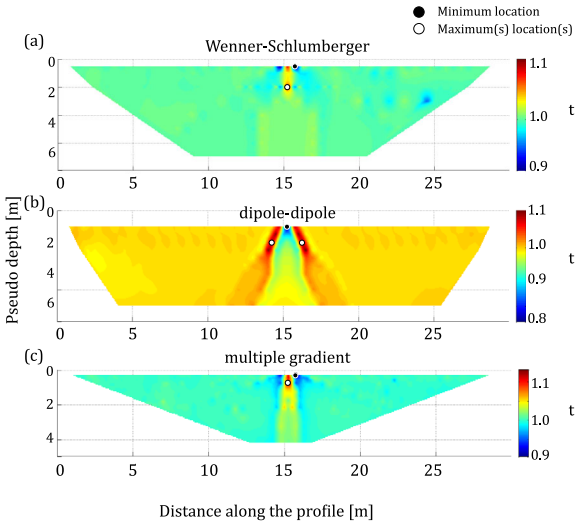

Figure 7. Topographic effect (t) computed for an interelectrode spacing of 0.50 m, a α ratio equal to 0.25 and a β ratio equal to 2/3, for the (a) WS, (b) DD and (c) GRAD arrays. The locations of minimum and maximum(s) of the resistivity values are indicated by dots.

the α ratio can be considered as a variation of the fissure size for a constant electrode spacing, or a variation of the electrode spacing for a fixed fissure size. Therefore, this sensitivity study on the α ratio only investigates the scale effect on the apparent resistivity values.

The previous reference fissure model is used with the same acquisition geometry. The fissure depth is first calculated from the known interelectrode spacing and the ratio α is selected. Then, its width is computed from the previously calculated depth and from the constant ratio β equals to 1.5.

Results indicate that, for the range of fissures tested numerically, the topographic effect anomaly is unchanged for a constant interelectrode spacing whatever the fissure size (with a constant fissure aspect ratio β) and the resistivity array used. Only the amplitude is changed, so that we can summarize the results by considering only the minimum and maximum topographic effect on the pseudo-section. The maxima and minima positions do not depend on the α ratios except for the DD configuration where the maximum can be located on each side of the symmetrical topographic anomaly (Fig. 7). This allows the determination of a critical α ratio ($C\alpha R$) for each resistivity array (Fig. 8). It is defined as the minimal α ratio for which the amplitude of the anomaly created by the fissure in the apparent resistivity, is greater than a 5 per cent. The $C\alpha R$ is lower for the DD than for the GRAD and WS arrays. Indeed, while the maximal topographic effect is equivalent for the three resistivity arrays, the minimal one decreases faster for the DD array, so that the $C\alpha R$ associated to the DD array $C\alpha R_{DD}$ is lower (0.095), compared to others $C\alpha R_{WS}$ and $C\alpha R_{GRAD}$, respectively equal to 0.155 and 0.160.

The numerical study confirms the higher sensitivity of the DD array to vertical structures (or to horizontal resistivity changes, Michot *et al.* 2003). For the reference fissure, the minimal fissure depth detectable is approximately equal to 0.1 times the interelectrode spacing for this resistivity array, and 0.16 times for the two other arrays. Although the $C\alpha R$ calculated depends on the threshold (defined at 5 per cent), the ratio $C\alpha R_{WS\text{-}GRAD}/C\alpha R_{DD}$ is substantially identical for a threshold of 10 per cent, namely 1.6.

A complementary detailed sensitivity study investigating the sensitivity of the three resistivity arrays to the different fissure

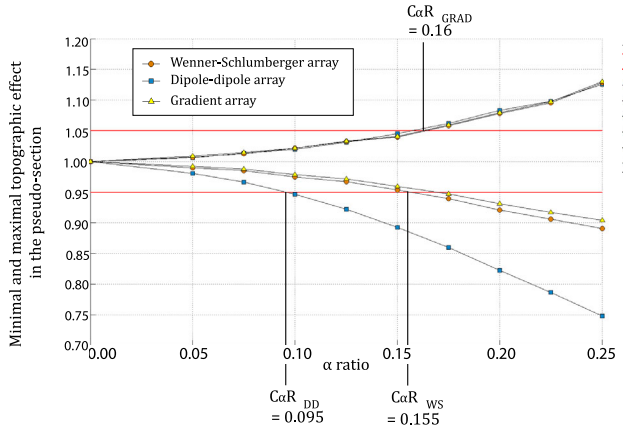

Figure 8. Minimal and maximal topographic effect in the pseudo-sections for different α ratios. The critical α ratio (CαR) computed for dipole–dipole (DD), gradient (GRAD) and Wenner–Schlumberger (WS) arrays are calculated as the first α ratio for which the topographic effect change is greater than 5 per cent.

descriptors is presented in Appendix B. It shows that fissure depth and position are the major parameters affecting the topographic effect, and therefore the apparent resistivity for the three arrays. Fissure width and dip angle have less importance (at least for the range of tested parameter values) on the topographic effect anomaly amplitude. These results demonstrate the necessity to measure accurately in the field the fissure depth and location for all fissures deeper than 0.1 times the interelectrode spacing while the fissure width and dip angle can be measured more roughly for fissure characterized by dimensions close to the reference fissure.

5 CORRECTION OF THE FISSURE EFFECT ON A REAL DATA SET

The controlled infiltration monitoring experiment described in Section 2 consists in infiltrating a low conductive water (2.3 µS cm^{-1}) pumped from a spring located upslope from the landslide, along an infiltration line perpendicular to the acquisition profile (Fig. 2a). It is constituted of three porous pipes (10 m in length), distributing slowly pumped stream water (Fig. 1a). The infiltration line is located between electrodes 20 and 21, at the abscissa $x = 9.7$ m. Several fissures cross the profile, with different sizes and orientations (Fig. 2a). One particular fissure is located just 0.1 m downslope of the infiltration line. Although all the fissures are not exactly perpendicular to the acquisition profile, we assume the experiment to be 2-D.

Three specific acquisitions are used in this work. The first two have been realized just before the start of the infiltration using a WS and a DD configuration. Then, 700 l of water have been injected through the porous pipes during 9 hours at a mean infiltration rate of 1.3 l min^{-1}. The barrel used to store water was emptied at midnight and the second acquisition has been carried out 9 hr after with a DD configuration. Additional measurements were realized during the infiltration. A humidity probe was installed 1.5 m downslope the infiltration (at 1 m depth) but did not record significant increase of humidity. The subsoil temperature (at 0.3 m) differs from less than 1 °C between the two acquisitions.

The purpose of this section is not to interpret the results in term of hydrological process, but rather to illustrate previous work on a real data set by correcting the effect of fissure on a real data set.

5.1 Apparent-resistivity correction

Using the topography measured by GPS (Fig. 9a) and the fissure geometry obtained from the surface fissure survey (Fig. 2a), we construct a mesh of the slope including vertical fissures (Fig. 9b).

We then compute numerically the geometrical factors k and the topographic effect from eq. (3) (Figs 10b and e). Finally, by dividing the apparent resistivity pseudo-section of the first data set (Figs 10a and d) by the topographic effect pseudo-section, we obtain the apparent resistivity pseudo-section corrected from the topographic effect (Figs 10c and f).

Although some artefacts are still present for abscissa greater than 20 m, a simple surface fissure survey allows to remove much topographic effect. The representation of the topographically corrected apparent resistivity allows a better representation of the soil resistivity, which is apparently rather homogeneous and low, ranging mainly between 30 and 40 Ωm. This range is typical of the Super-Sauze reworked black marls (Travelletti & Malet 2012). This correction would have also allowed to observe any anomaly that was previously hidden by surface fissure effect. Some residual resistive anomalies are visible in the lower part of the slope, where fissures are larger and present complex geometries.

5.2 Static inversion of corrected apparent resistivity

The previous sections were dedicated to the analysis of the apparent resistivity sensitivity to different fissure descriptors and to the correction of apparent resistivity from the effect of fissure. However, apparent resistivity pseudo-sections only give a first-order information of the subsoil structure. A more detailed interpretation requires data inversion. Therefore, the next step of this work consists in assessing the contribution of the surface fissure correction on the inversion. It consists in inverting the same initial data set using three different methods. The BERT2 inversion code (Günther *et al.* 2006) is used to invert the data set acquired with a DD configuration before the infiltration, according these three different strategies of inversion:

(i) *Strategy of inversion 1:* This 'classic' strategy of inversion is used to present the preliminary results on fissure effects on resistivity (Fig. 2b). It consists in inverting the raw apparent resistivity (Fig. 10a), simply using the topography measured by GPS at each electrode, without considering any fissure geometry (Figs 11b and 12b).

(ii) *Strategy of inversion 2:* This second inversion strategy consists in inverting the data set corrected from fissure effects (see Fig. 10c). The fissure geometry has been included in the forward computing mesh but the topography used for the inversion mesh

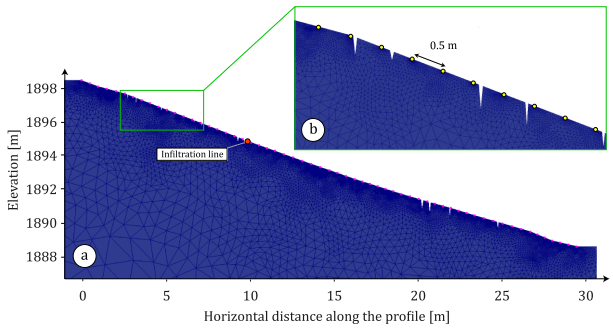

Figure 9. Mesh used for the computation of the true geometrical factor k_{true}.

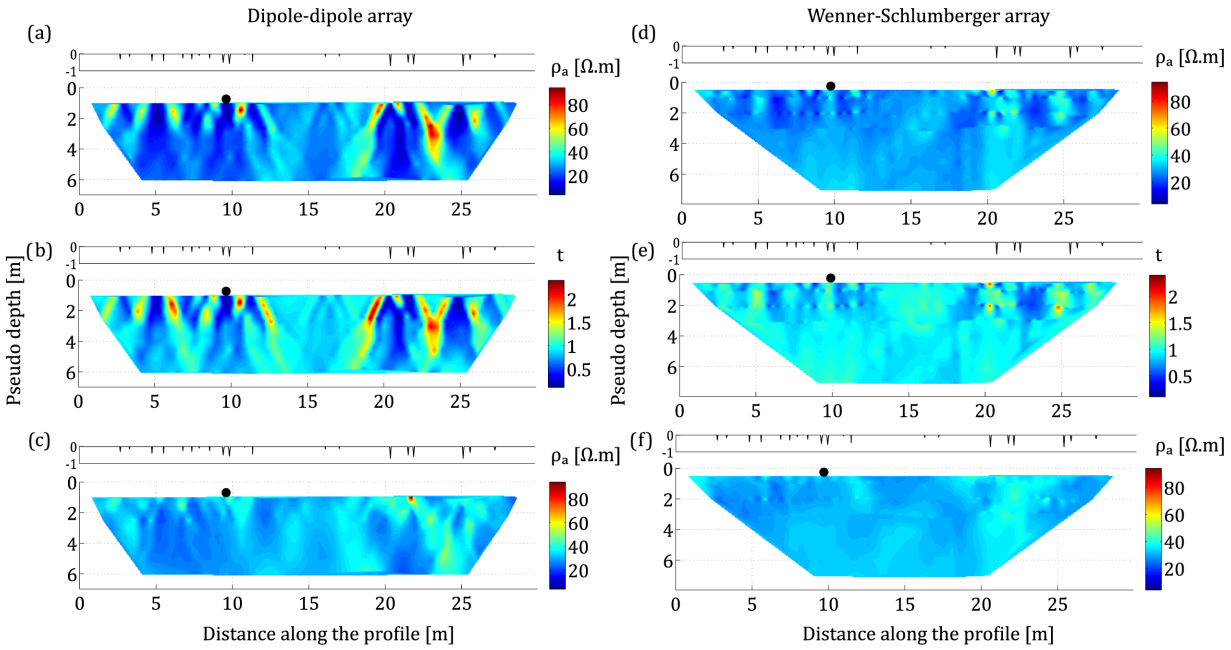

Figure 10. Correction of the fissure effect on the apparent resistivity pseudo-section on real data sets acquired before the infiltration with DD (left-hand panels) and WS (right-hand panels) configurations: (a) and (d) pseudo-sections of apparent resistivity acquired before the infiltration and calculated with eq. (1), (b) Pseudo-section of topographic effect t calculated with eq. (3) using the model constructed from the surface fissure survey (Fig. 9) and (c) pseudo-section of corrected apparent resistivity, that is raw apparent resistivity divided by the topographic effect t. The infiltration line is represented as a black dot.

is the same as inversion 1 (i.e. the one measured by GPS at each electrode position). The advantage of this type of inversion is that it only requires the use of an arbitrary-topography forward dc resistivity modelling code to correct for the fissure artefacts from the pseudo-section. Then, the corrected data set can be inverted with any inversion code, not particularly adapted for arbitrary topography (Figs 11c and 12c).

(iii) *Strategy of inversion 3:* This inversion strategy consists in inverting the raw apparent resistivity by incorporating the fissure geometry in the primary mesh (used for forward modelling and Jacobian matrix computing) and in the inversion mesh (which contains the inverted soil resistivity). Thereby, contrary to inversion 2, the Jacobian matrix, used in the residual retro-propagation, accounts for the presence of surface fissures. This inversion requires the use of an arbitrary-topography adapted inversion code such as BERT2 (Figs 11d and 12d).

The principal inversion parameters used for the three inversions are detailed in Table 3. Following Günther *et al.* (2006) we impose an error on the data calculated as the sum of a constant percentage (3 per cent) and a relative voltage error measured as the standard deviation on voltage measurement by the resistivimeter. Both L_1 and L_2 norms on the data are used. The RMSE and χ^2 values resulting from the inversions are indicated Table 4.

The χ^2 parameter defines the mean squared error relatively to the data error. A value close to 1 indicates that data are not overfitted. These value indicate *a priori* a slight improvement of the result with inversions 2 or 3, compared to inversion 1 for $L1$ and $L2$ norms. The reader has to be aware of the low sensitivity of ERT in depth for clayey soil, whatever the geometry and the array used. In the presented section, the sensitivity strongly decreases below 0.7 m in depth, so that the section only represents a blurred image of the reality below this depth. However, the deep anomaly patterns created by the inversion process are just as interesting as the surface resistivity changes. Therefore, for sake of clarity, the sensitivity is voluntarily not shown in the results of the three inversions in Figs 11(b)–(d) for the $L1$ norm and in Figs 12(b)–(d) for the $L2$ norm.

The tomographies obtained from the classical inversions (inversion strategy 1) using $L1$ and $L2$ norms show resistive anomalies at the surface associated to the presence of fissures, as discussed in Section 2. Other resistive and conductive anomalies not linked to anomalies in the apparent resistivity, nor to the presence of fissures on the ground are visible both in depth (zone 1) and at the surface (zone 2). They are interpreted as inversion artefacts, certainly due to the presence of the resistive fissure anomalies, and confirmed by synthetic tests not presented here. This type of artefacts have also been observed in Sentenac & Zielinski (2009).

The strategy of inversion 2 and 3, that account for the correction of the surface fissure effect, allow for strongly mitigating the resistive anomalies associated to the presence of surface fissure for both $L1$ and $L2$ norms, although in the lower part of the profile, where the correction of surface fissure on apparent resistivity is poorer, some of these anomalies are still present.

One can also notice the mitigation of the inversion artefacts. They have almost completely disappeared at the surface in zone 2 and the amplitude of the conductive anomaly located in depth in zone 1 has decreased for about −40 per cent with the $L1$ norm and for −27 per cent for the $L2$ norm.

Although the inversion strategies 2 and 3 strongly improve the results, particularly in the upper part of the slope, we observe some difference between the use of $L1$ and $L2$ norms. The use of the $L2$ norms allows to invert the electrical resistivity with a RMSE closer to the uncertainty on the measurements but also results in smooth and spread inversion artefacts. Contrariwise, the use of the $L1$ norm results in higher RMSE (11 per cent compared to 7 per cent) and in more punctual inversion artefacts. This difference is particularly visible in the lower part of the profile, where the residual inversion artefacts are more important (number, width and amplitude) for the $L2$ norm.

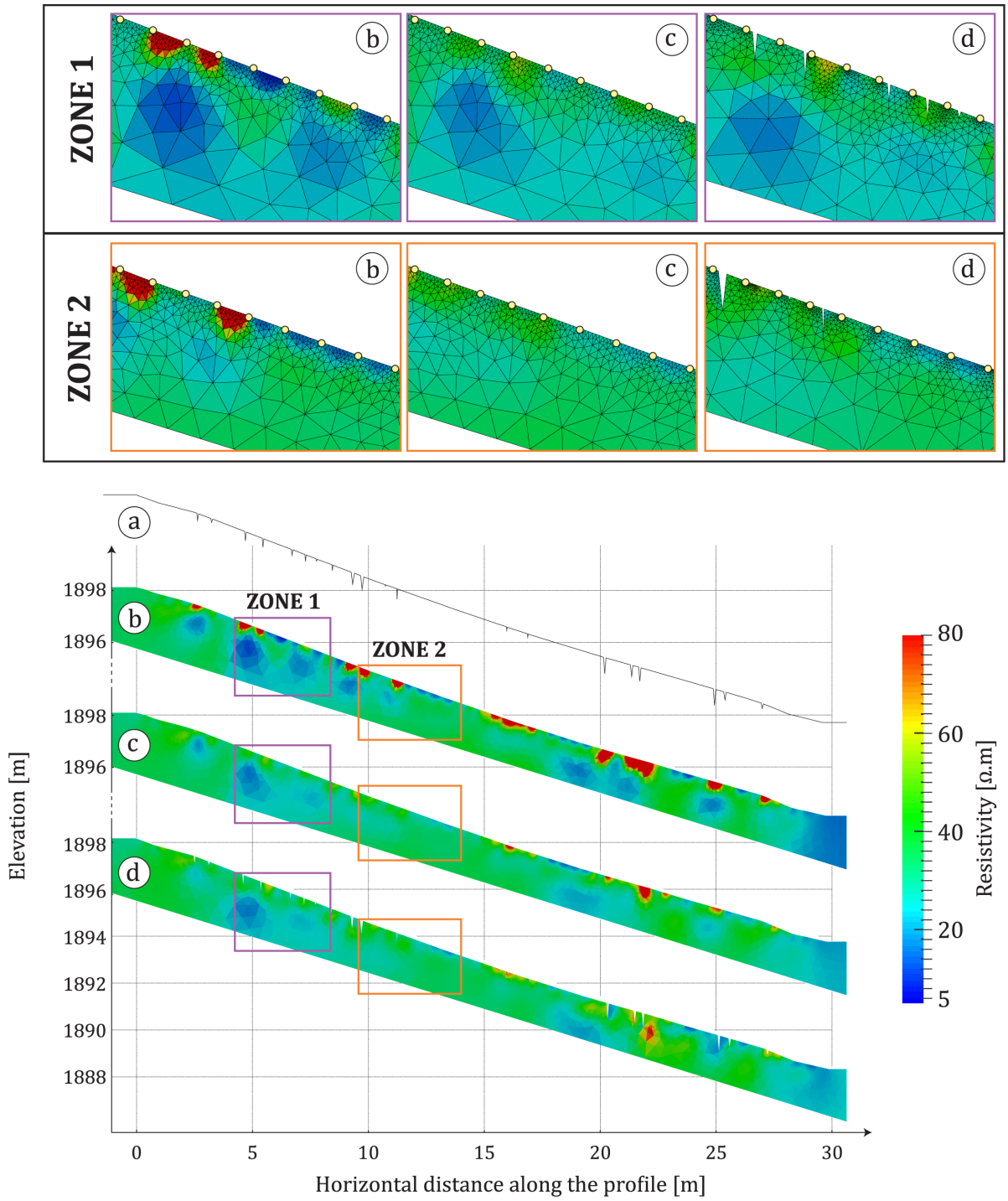

Figure 11. Results of the static inversion for the three different strategies using the $L1$ norm on data. (a) Mesh containing surface fissure geometries used for the correction of apparent resistivity, (b) result of the inversion with strategy 1: inversion of the raw data set only considering the topography measured by GPS at each electrode position, (c) result of the inversion with strategy 2: inversion of the data set corrected from surface fissure effects on the topography measured by GPS at each electrode position and (d) result of the inversion with strategy 3: inversion of raw the data set on meshes containing the surface fissure geometry (forward and inverse modelling). The close-ups of the zones 1 and 2 of the inverted tomographies are also presented with the mesh.

The static inversion of a data set in the presence of surface fissure can be improved with our methodology. The mitigation of large resistive anomalies in the topsoil also affects the deeper part of the section. However due to a poor knowledge and a strong approximation of the fissure geometry, these inversion artefacts are not totally suppressed (see close-ups in Figs 11 and 12). In this context, a change of the soil resistivity distribution with time (e.g. due to a change of soil water content) could result in a change of the residual inversion artefact distribution and still prevent from performing ERT monitoring. Therefore, in the next section, we study the contribution of our methodology to improve the time-lapse inversion results on fissured media.

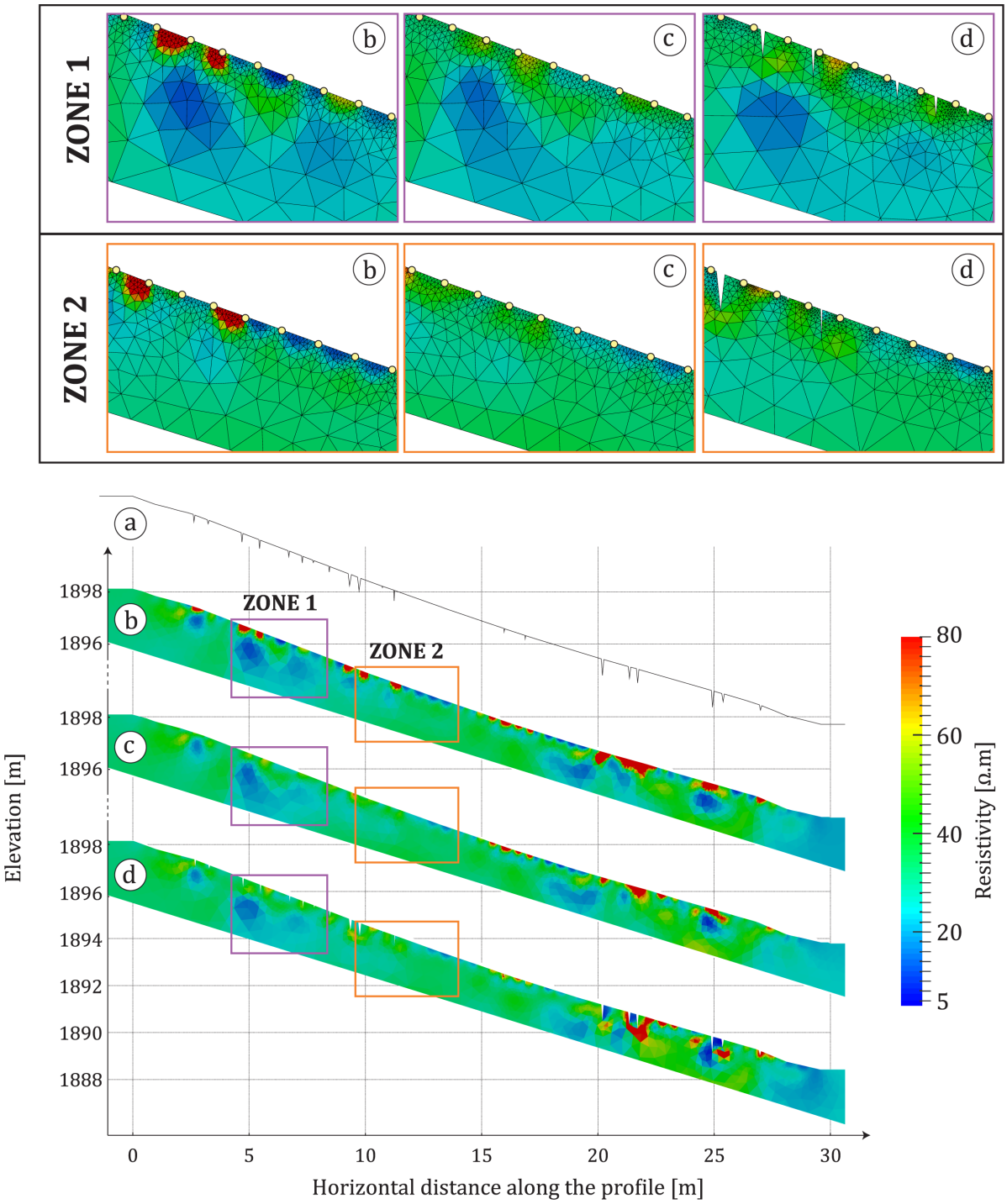

Figure 12. Results of the static inversion for the three different strategies using the *L*2 norm on data. (a) Mesh containing surface fissure geometries used for the correction of apparent resistivity, (b) result of the inversion with strategy 1: inversion of the raw data set only considering the topography measured by GPS at each electrode position, (c) result of the inversion with strategy 2: inversion of the data set corrected from surface fissure effects on the topography measured by GPS at each electrode position and (d) result of the inversion with strategy 3: inversion of raw the data set on meshes containing the surface fissure geometry (forward and inverse modelling). The close-ups of the zones 1 and 2 of the inverted tomographies are also presented with the mesh.

5.3 Time-lapse inversion of corrected apparent resistivities

Residual effects of fissures in the corrected pseudo-section certainly come from the combination of several factors. Their complete manual removing is impossible. In this condition, the selection of appropriate inversion parameters could allow to attenuate the amplification of these artefacts in the inverted resistivity section, and could allow for monitoring water flux around fissures with ERT. Therefore, we perform a time-lapse inversion by adopting the following parameters. They are chosen with the aim of reducing the anomaly spreading in the inverted resistivity section and decreasing

Table 3. Inversion parameter used for the different inversions.

Parameter	Comment	Value
PARADX	Relative parameter mesh refinement at the surface	1/10 interelectrode spacing
PRIMDX	Primary mesh refinement	0.01 m
BLOCKYMODEL	Norm used on model	0 (L_2 norm)
λ	Damping factor	20
ZWEIGHT	Flatness ratio	1.0
MAXITER	Maximal number of iteration	20

Table 4. The rms errors and χ^2 values associated to the different inversions.

	Inversion 1	Inversion 2	Inversion 3
L1 norm	RMSE = 52.9 per cent $\chi^2 = 1.0$	RMSE = 10.4 per cent $\chi^2 = 0.8$	RMSE = 11.3 per cent $\chi^2 = 0.9$
L2 norm	RMSE = 7.2 per cent $\chi^2 = 3.0$	RMSE = 4.1 per cent $\chi^2 = 1.5$	RMSE = 7.0 per cent $\chi^2 = 4.4$

Table 5. The rms and absolute errors related to the different inversions.

Data set	Inversion 1	Inversion 2	Inversion 3
Before the infiltration	ABS = 34.8 per cent rms = 58.7 per cent $\chi^2 = 3.0$	ABS = 25.3 per cent rms = 39.2 per cent $\chi^2 = 1.5$	ABS = 11.3 per cent rms = 18.0 per cent $\chi^2 = 1.9$
After the infiltration	ABS = 34.1 per cent rms = 58.0 per cent $\chi^2 = 2.5$	ABS = 25.3 rms = 40 per cent $\chi^2 = 2.0$	ABS = 11.4 per cent rms = 17.9 per cent $\chi^2 = 3.1$

the sensitivity of the inversion process to large apparent resistivity data.

With regards to the literature (Sentenac & Zielinski 2009; Jones *et al.* 2012) and our conclusion on the ability of the $L1$ norm on the data to reduce the artefact spreading; we invert the two data sets acquired before and after the infiltration experiment using this norm. This norm is generally used for the same reasons in this context (Sentenac & Zielinski 2009; Jones *et al.* 2012). To minimize the spreading of the inversion artefacts in the model, we also use the $L1$ norm on the model.

Then, to minimize the focusing of the inversion process on surface fissure anomaly we used a mix between first and zeroth order smoothness constrain on the reference model for the first data set and during time-lapse inversion. This option reduce the smoothing and avoids very large resistivity values by constraining the convergence toward a model close to a reference model. The reference model is a homogeneous model (30 Ωm) for the inversion of the first data set and is the result of the first inversion for the second data set. The model functional to be minimized is expressed in eq. (5) (Günther *et al.* 2006).

$$\Phi_m = \left[\|C(m - m_0)\|_1 + \alpha \|(m - m_0)\|_1\right], \quad (5)$$

where m and m_0 are the current and reference models, C a first-order smoothness matrix and α a fixed coefficient defined at a value of 0.2 by Günther *et al.* (2006). The other inversion parameters are unchanged (Table 3). The RMSE, absolute errors and χ^2 values associated to the different inversions are gathered in Table 5.

Inversion results are presented in Fig. 13 as percentage changes of resistivity relatively to the tomography acquired before the infiltration. The three inversion results are quite different the ones from the others, but we can distinguish on any of them a significant conductive anomaly starting near the infiltration line with negative maximal amplitudes of 20 per cent depending on the inversion. Although we reduced the smoothing constrain on the model, this anomaly is continuous (not crossed by high resistive anomaly) and more spread for the three inversion results, than when using classical inversion parameters. It seems that even using these particular inversion parameters, the inversion remains sensitive to the slight changes of resistivity around the fissures than to the decrease of resistivity due to water infiltration. These difficulties are compounded by the changes of apparent resistivity (∼20 per cent) around the fissures. These changes can be explained by water evaporation from surface fissure and/or by the closing of fissure during the two acquisitions. The shape of the wetting front observed for inversion 3 is the most probable. It is also coherent with the existence of transversal water flows through the fissure network, explaining the small size of the wetting front at the foot of the fissure despite the amount of water infiltrated, and also the fact that no change of soil water content has been detected with the humidity probe located 1-m downslope the infiltration line.

This last result is only illustrative. The large error resulting from the inversions make them unreliable and do not permit any safe interpretation. Nevertheless, it seems to prove that better results could be obtain with an appropriate selection of inversion parameters and also maybe using specifically developed inversion algorithm.

6 DISCUSSION AND CONCLUSION

This work focused on the effect of surface fissures on the apparent resistivity measurements, for fissures characterized by dimensions lower than the interelectrode spacing and almost parallel to the direction of the measurement profile. At this stage of development,

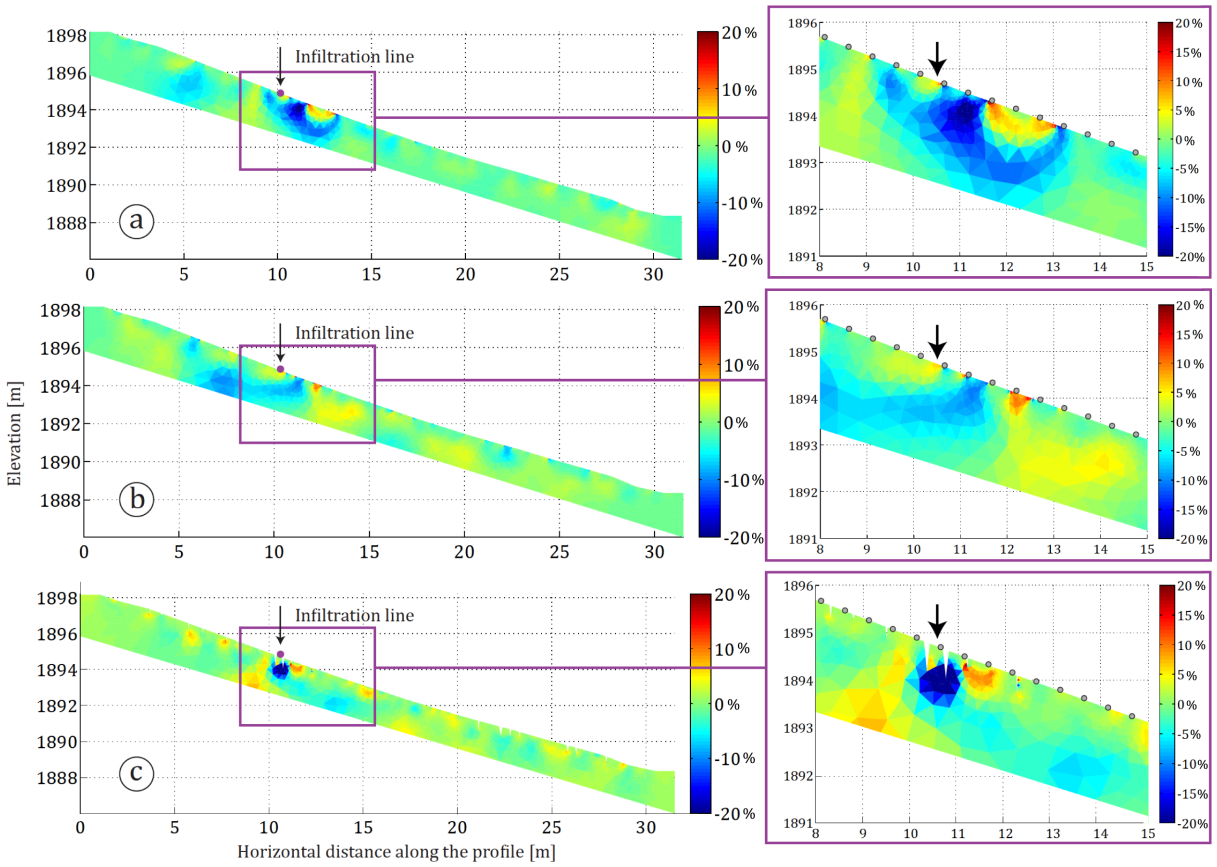

Figure 13. Results of the time-lapse inversion for the three different strategies using the $L1$ norm on the model and data and using a mix between first and zeroth order smoothness constrain on the homogeneous reference model. (a) Result of the time-lapse inversion with strategy 1: inversion of the raw data set only considering the topography measured by GPS at each electrode position, (b) results of time-lapse inversion with strategy 2: inversion of the data set corrected from surface fissure effects on the topography measured by GPS at each electrode position and (c) result of the time-lapse inversion wit strategy 3: inversion of raw the data set on meshes containing the surface fissure geometry (forward and inverse modelling). For each result, a close-up view of the section around the infiltration line is shown.

our work is limited to a narrow range of crack/fissure geometry. The goal of this exploratory study was to illustrate the issues of surface fissures for ERT measurements through the analysis of a case study. Although it is outside of the scope of this work, the extension to three dimensions would allow to enlarge the range of fissures for which the method is suitable.

A sensitivity analysis has been performed to assess the effect of each fissure descriptor. The results of this work are presented in terms of pseudo-sections of apparent resistivity to facilitate the interpretation of real data. The conclusions of the sensitivity analysis are the following:

(i) It confirms the high sensitivity of the DD array compared to WS and GRAD arrays.

(ii) The pattern of the topographic effect is not modified for the range of fissure descriptors used in this study (Table 1) and for three common resistivity arrays; only the amplitudes are affected.

(iii) The anomaly created by the fissure is symmetric for the three arrays except for fissures not centred in-between two electrodes or characterized by large dipping.

(iv) The fissure opening width and dip angles have little impact compared to the fissure depth which may affect the apparent resistivity values for more than 200 per cent.

(v) The fissure filling by water removes the topographic effect, linearly with the percentage of filling. The presence of a highly conductive water in the fissure tends to minimize this effect.

(vi) For a fissure width equal to 0.20 m, the anomaly in the pseudo-section exceed 5 per cent at fissure depth equal to 0.10 times the interelectrode spacing for a DD array and 0.15 for a GRAD and WS arrays.

We show that a simple fissure survey allows to correct for the complex pattern of artefacts observed in the pseudo-section. Considering that apparent resistivity pseudo-sections are generally related to the distribution of true soil resistivity (Griffiths & Barker 1993), this correction allows a first interpretation without inversion (Nicollin *et al.* 2006). Moreover, the correction of surface fissure effect largely improves the inverted resistivity section by attenuating the resistive anomalies in the topsoil and by minimizing anomalies resulting from inversion artefacts. It seems that the anomalies inverted on a mesh containing the fissure geometry are better located in depth.

For the real case data set, residual errors on the fissure geometry create small residual anomalies in the corrected pseudo-section that are amplified by the inversion. Thereby, small resistive anomalies and their associated inversion artefacts are present in the inverted resistivity section. The results could be improved by using a semi-automatic fissure shape inversion from apparent resistivity pseudo-section (Wilkinson *et al.* 2010). The main difficulty expected come from the ill-posedness of the inverse problem is that several sets of fissure descriptor can produce the same topographic effect. However, this study shows that some resistivity arrays show

very different behaviour to certain parameter, like DD and GRAD arrays. Therefore, we anticipate to better constrain the problem by using multiple array measurements. Similarly, research could be emphasized on the selection of specific inversion parameters or on the development of inversion strategies dedicated to the inversion of data sets acquired on fissured ground.

ACKNOWLEDGEMENTS

This work was part of the OMIV project 'Observatoire Multidisciplinaire des Instabilités de Versants' and was financially supported by the BRGM Carnot Institute. The authors thank Thomas Günther (Leibniz Institute for Applied Geophysics, Hannover) for providing the DC-FEM forward modelling code and usage tips adapted to this numerical study, as well as the two anonymous reviewers for their helpful comments and recommendations.

REFERENCES

Amato, M., Basso, B., Celano, G., Bitella, G., Morelli, G. & Rossi, R., 2008. In situ detection of tree root distribution and biomass by multi-electrode resistivity imaging, *Tree Physiol.,* **28**(10), 1441–1448.

Amidu, S.A. & Dunbar, J.A., 2007. Geoelectric studies of seasonal wetting and drying of a texas vertisol, *Vadose Zone J.,* **6**(3), 511–523.

Besson, A., Cousin, I., Samouëlian, A., Boizard, H. & Richard, G., 2004. Structural heterogeneity of the soil tilled layer as characterized by 2D electrical resistivity surveying, *Soil Tillage Res.,* **79**(2), 239–249.

Bobachev, A.A., Marchenko, M.N., Modin, I.N., Pervago, E.V., Urusova, A.V. & Shevnin, V.A., 1995. New approaches to electrical soundings of horizontally inhomogeneous media, *Izvest. Phys. Solid Earth,* **31,** 1075–1086.

Clément, R., Oxarango, L. & Descloitres, M., 2011. Contribution of 3-D time-lapse ERT to the study of leachate recirculation in a landfill, *Waste Manag.,* **31**(3), 457–467.

Dahlin, T. & Zhou, B., 2006. Multiple-gradient array measurements for multichannel 2D resistivity imaging, *Near Surf. Geophys.,* **4**(2), 113–123.

Dinka, T.M., 2012. Review paper: challenges and limitations in studying the shrink-swell and crack dynamics of vertisol soils, *Open J. Soil Sci.,* **02**(02), 82–90.

Espinosa, A.A., 2009. Analysis and quantification of preferential flow on the super Sauze landslide, *MSc thesis,* TU Delft.

Ferahtia, J., Djarfour, N., Baddari, K. & Guérin, R., 2009. Application of signal dependent rank-order mean filter to the removal of noise spikes from 2D electrical resistivity imaging data, *Near Surf. Geophys.,* **7**(3), 159–169.

Gance, J., Grandjean, G., Samyn, K. & Malet, J.-P., 2012. Quasi-newton inversion of seismic first arrivals using source finite bandwidth assumption: application to subsurface characterization of landslides, *J. appl. Geophys.,* **87,** 94–106.

Grandjean, G., Bitri, A. & Krzeminska, D.M., 2012. Characterisation of a landslide fissure pattern by integrating seismic azimuth tomography and geotechnical testing, *Hydrol. Process.,* **26**(14), 2120–2127.

Greve, A., Andersen, M. & Acworth, R., 2012. Monitoring the transition from preferential to matrix flow in cracking clay soil through changes in electrical anisotropy, *Geoderma,* **179–180,** 46–52.

Greve, A.K., Acworth, R.I. & Kelly, B.F., 2010. Detection of subsurface soil cracks by vertical anisotropy profiles of apparent electrical resistivity, *Geophysics,* **75**(4), WA85–WA93.

Griffiths, D.H. & Barker, R.D., 1993. Two-dimensional resistivity imaging and modelling in areas of complex geology, *J. appl. Geophys.,* **29**(3), 211–226.

Günther, T., Rücker, C. & Spitzer, K., 2006. Three-dimensional modelling and inversion of dc resistivity data incorporating topography–II. inversion, *Geophys. J. Int.,* **166**(2), 506–517.

Jackson, P.D., Northmore, K.J., Meldrum, P.I., Gunn, D.A., Hallam, J.R., Wambura, J., Wangusi, B. & Ogutu, G., 2002. Non-invasive moisture monitoring within an Earth embankment—a precursor to failure, *NDT E Int.,* **35**(2), 107–115.

Jones, G., Sentenac, P. & Zielinski, M., 2012. Fissure detection in flood embankments using electrical resistivity tomography, in *Proceedings of the Near Surface Geoscience 2012—18th European Meeting of Environmental and Engineering Geophysics*.

Jung, H.K. & Park, C., 2005. Geophysical resistivity imaging for upper layer of shield TBM tunnel ceiling, *Geosyst. Eng.,* **8**(3), 83–87.

Krzeminska, D.M., Bogaard, T.A., van Asch, Th.W.J. & van Beek, L.P.H., 2011. A conceptual model of the hydrological influence of fissures on landslide activity, *Hydrol. Earth Syst. Sci. Discuss.,* **8**(6), 11 039–11 073.

Lataste, J., Sirieix, C., Breysse, D. & Frappa, M., 2003. Electrical resistivity measurement applied to cracking assessment on reinforced concrete structures in civil engineering, *NDT E Int.,* **36**(6), 383–394.

Loke, M.H., 2000. Topographic modelling in electrical imaging inversion, in *Proceedings 62nd Meeting of the European Association of Exploration Geoscientists,* Glasgow, Scotland, pp. 1–4.

Loke, M. & Barker, R., 1996. Rapid least-squares inversion of apparent resistivity pseudo-sections by a quasi-newton method 1, *Geophys. Prospect.,* **44**(1), 131–152.

Michot, D., Benderitter, Y., Dorigny, A., Nicoullaud, B., King, D. & Tabbagh, A., 2003. Spatial and temporal monitoring of soil water content with an irrigated corn crop cover using surface electrical resistivity tomography, *Water Resour. Res.,* **39**(5), 1138, doi:10.1029/2002WR001581.

Nicollin, F., Gibert, D., Beauducel, F., Boudon, G. & Komorowski, J.-C., 2006. Electrical tomography of la Soufrière of Guadeloupe volcano: field experiments, 1D inversion and qualitative interpretation, *Earth planet. Sci. Lett.,* **244**(3–4), 709–724.

Niethammer, U., James, M., Rothmund, S., Travelletti, J. & Joswig, M., 2012. UAV-based remote sensing of the super-Sauze landslide: evaluation and results, *Eng. Geol.,* **128,** 2–11.

Ritz, M., Robain, H., Pervago, E., Albouy, Y., Camerlynck, C., Descloitres, M. & Mariko, A., 1999. Improvement to resistivity pseudo-section modelling by removal of near-surface inhomogeneity effects: application to a soil system in South Cameroon, *Geophys. Prospect.,* **47**(2), 85–101.

Robert, T., Caterina, D., Deceuster, J., Kaufmann, O. & Nguyen, F., 2012. A salt tracer test monitored with surface ERT to detect preferential flow and transport paths in fractured/karstified limestones, *Geophysics,* **77**(2), B55–B67.

Rots, J. & Blaauwendraad, J., 1989. Crack models for concrete, discrete or smeared? Fixed, multi-directional or rotating?, *Delft University of Technology*.

Rücker, C., Günther, T. & Spitzer, K., 2006. Three-dimensional modelling and inversion of dc resistivity data incorporating topography - I. modelling, *Geophys. J. Int.,* **166**(2), 495–505.

Sambridge, M., Braun, J. & McQueen, H., 1995. Geophysical parametrization and interpolation of irregular data using natural neighbours, *Geophys. J. Int.,* **122**(3), 837–857.

Samouëlian, A., Cousin, I., Richard, G., Tabbagh, A. & Bruand, A., 2003. Electrical resistivity imaging for detecting soil cracking at the centimetric scale, *Soil Sci. Soc. Am. J.,* **67**(5), 1319–1326.

Samouelian, A., Richard, G., Cousin, I., Guerin, R., Bruand, A. & Tabbagh, A., 2004. Three-dimensional crack monitoring by electrical resistivity measurement, *Eur. J. Soil Sci.,* **55**(4), 751–762.

Scollar, I., Tabbagh, A., Hesse, A. & Herzog, I., 1990. *Archaeological Prospecting and Remote Sensing,* Cambridge Univ. Press.

Sentenac, P. & Zielinski, M., 2009. Clay fine fissuring monitoring using miniature geo-electrical resistivity arrays, *Environ. Earth Sci.,* **59**(1), 205–214.

Srayeddin, I. & Doussan, C., 2009. Estimation of the spatial variability of root water uptake of maize and sorghum at the field scale by electrical resistivity tomography, *Plant Soil,* **319**(1–2), 185–207.

Stumpf, A., Malet, J.-P., Kerle, N., Niethammer, U. & Rothmund, S., 2013. Image-based mapping of surface fissures for the investigation of landslide dynamics, *Geomorphology,* **186,** 12–27.

Suzuki, K. & Higashi, S., 2001. Groundwater flow after heavy rain in landslide-slope area from 2-D inversion of resistivity monitoring data, *Geophysics,* **66**(3), 733–743.

Tabbagh, J., Samouëlian, A., Tabbagh, A. & Cousin, I., 2007. Numerical modelling of direct current electrical resistivity for the characterisation of cracks in soils, *J. appl. Geophys.,* **62**(4), 313–323.

Travelletti, J. & Malet, J.-P., 2012. Characterization of the 3D geometry of flow-like landslides: a methodology based on the integration of heterogeneous multi-source data, *Eng. Geol.,* **128,** 30–48.

Travelletti, J., Sailhac, P., Malet, J.-P., Grandjean, G. & Ponton, J., 2012. Hydrological response of weathered clay-shale slopes: water infiltration monitoring with time-lapse electrical resistivity tomography, *Hydrol. Process.,* **26**(14), 2106–2119.

Tsourlos, P.I., Szymanski, J.E. & Tsokas, G.N., 1999. The effect of terrain topography on commonly used resistivity arrays, *Geophysics,* **64**(5), 1357–1363.

Van Asch, T., Buma, J. & Van Beek, L., 1999. A view on some hydrological triggering systems in landslides, *Geomorphology,* **30**(1), 25–32.

Velde, B., 1999. Structure of surface cracks in soil and muds, *Geoderma,* **93**(1), 101–124.

Wilkinson, P.B., Chambers, J.E., Meldrum, P.I., Gunn, D.A., Ogilvy, R.D. & Kuras, O., 2010. Predicting the movements of permanently installed electrodes on an active landslide using time-lapse geoelectrical resistivity data only, *Geophys. J. Int.,* **183**(2), 543–556.

APPENDIX A: RESISTIVITY ARRAY DESCRIPTION

The sequences of the three resistivity arrays are defined in Table A1. They can be summarized using three parameters *a*, *n* and *s*. Parameter *a* defines the minimal dipole size in a minimal interelectrode spacing unit (here 0.5 m), the parameter *n* defines the quadripole length for the WS and DD array. The *a*, *s* and *n* parameters of the multiple gradient array are represented in Fig. A1.

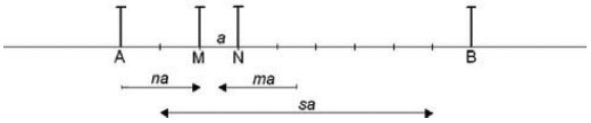

Figure A1. Multiple gradient array parameters definition from Dahlin & Zhou (2006). *a*, is the potential measurement dipole, *s* is the separation factor, here equal to 7, *n* is the factor defining the smallest relative spacing between a current and a potential electrode (always equal to 1 in this study).

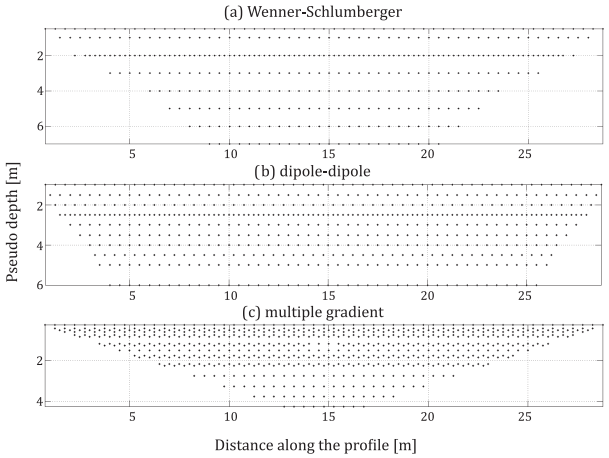

Figure A2. Measurement positions represented on the pseudo-sections for the three resistivity arrays: (a) Wenner–Schlumberger, (b) dipole–dipole and (c) multiple gradient.

The position of the measurement points is represented in Fig. A2 for the three resistivity arrays.

APPENDIX B: DETAILED RESULTS OF THE SENSITIVITY ANALYSIS

This appendix presents the supplementary results of the sensitivity analysis investigating the effect of different fissure descriptors on the apparent resistivity.

Table A1. Resistivity array description.

Array	*a*	*s*	*n*
WS	1	–	0.5 and 2
WS	2	–	0.5
WS	4	–	0.25, 0.5 and 0.75
WS	8	–	0.375, 0.5, 0.625, 0.75 and 0.875
Total number of measurements			**466**
DD	1	–	0.5, 1, 1.5 and 2
DD	2	–	0.75 and 1
DD	3	–	0.67
DD	4	–	0.5, 0.625, 0.75 and 1
Total number of measurements			**562**
GRAD	1	1, 3, 5 and 7	1
GRAD	2	7, 9 and 11	1
GRAD	3	11, 13, 15 and 16	1
Total number of measurements			**2511**

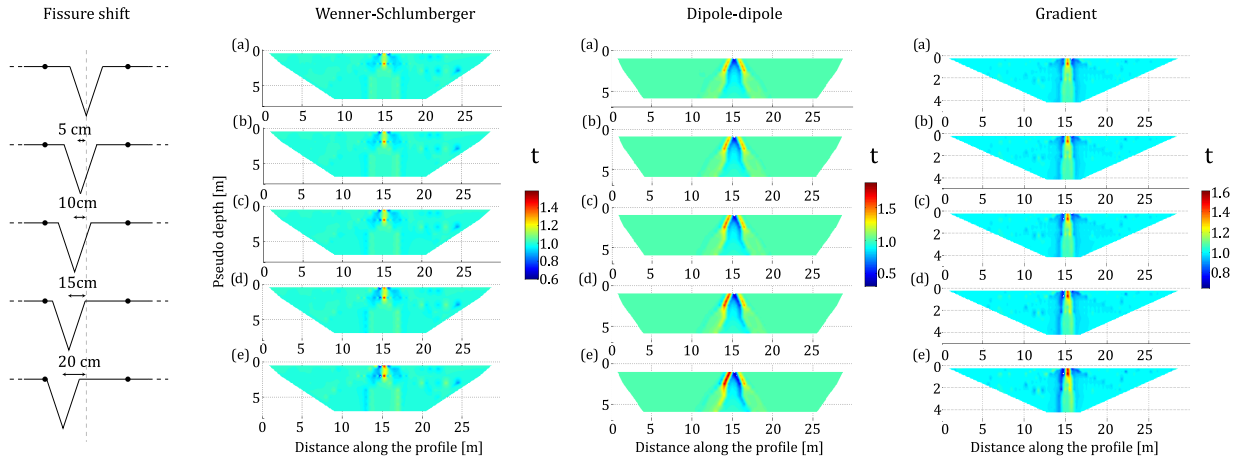

Figure B1. Pseudo-section of topographic effect (t) computed for different eccentric positions of the fissure for the WS, DD and GRAD arrays.

B1 Effect of the relative position of the fissure to the electrode on apparent resistivity

This experiment explores the effect of a fissure not centred between two electrodes. We compute the forward dc-electrical problem on a fissure characterized by a width of 0.10 m and a depth of 0.30 m. The fissure, thinner than the reference fissure, allow exploring the effect of a fissure shifted towards the left in the range 0–0.20 m. The results are presented in Fig. B1.

This shift results in an asymmetry of the topographic effect anomaly. This asymmetry is visible starting from a shift of 0.10 m on the DD and GRAD arrays, and 0.15 m on the WS array. It also results in the progressive increase of the topographic effect when the distance fissure-electrode decreases. The topographic effect can be multiplied by 2 between a fissure centred between a pair of electrodes and a fissure with an edge at an electrode position.

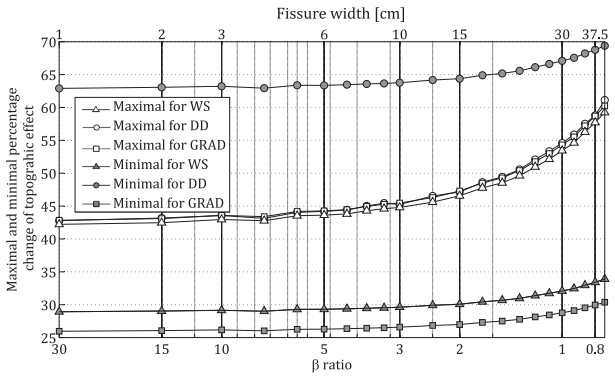

Figure B2. Maximal and minimal percentage change of topographic effect in the pseudo-section compared to an homogeneous half-space for different fissure opening and for a constant depth of 0.30 m, computed for the WS, DD and GRAD arrays.

B2 Effect of the fissure geometry

This experiment explores the sensitivity of the different arrays to the fissure geometry. In this section, the fissure to dipole size ratio α is kept constant whenever possible, and the fissure aspect ratio β is variable.

B2.1 Effect of fissure opening (e.g. width)

For this numerical experiment, a constant depth (0.30 m) of the reference fissure is used. The fissure width varies between 0.01 and 0.40 m for a β ratio variation ranging from 0.75 to 30. The pattern of the topographic effect is the same as previously. The results can be summarized by the maximal and minimal percentage change of the topographic effect in the pseudo-section, compared to a homogeneous half-space without fissure. They are presented in Fig. B2 for the three resistivity arrays.

The results indicate that the maximal percentage changes are almost identical for the three resistivity arrays ranging between 42 and 60 per cent, respectively, for a fissure width ranging between 0.01 and 0.40 m. They remain almost constant for β ratio lower than 3 (fissure width lower than 0.1 m in this particular case) and start increasing from this value. Contrary to the maximal percentage change, the minimal percentage change amplitude depends more on the resistivity array than on the fissure width.

B2.2 Effect of fissure depth

For this numerical experiment, a constant width (0.20 m) of the reference fissure is used. The fissure depth varies between 0.01 and 1.00 m and gives a β ratio variation ranging from 0.05 to 5. Although the interelectrode spacing is kept constant, the fissure to dipole size ratio α is variable because of the ratio definition. The maximal and minimal percentage change of topographic effect in the pseudo-section, compared to a homogeneous half-space, are presented in Fig. B3 for the three resistivity arrays.

At the contrary of the maximal change of topographic effect, the minimal change depends on the resistivity array. The DD array presents a minimal topographic effect equal to 0.04 for a fissure depth of 1 m. The apparent resistivity is therefore divided by a factor 25 giving a minimal anomaly percentage change of 96 per cent. The minimal topographic effect anomalies for GRAD and WS arrays are, respectively, 58 and 53 per cent for a fissure depth of 1 m. The maximal topographic effect anomaly is similar for the three arrays with a final maximal percentage change of 200 per cent for the DD array. An inflexion point can be noticed for a depth of 0.30 m for the maximal anomaly percentage change. This highlights the important effect of the fissure depth on the resistivity arrays, particularly for the DD array and for α ratios larger than 0.6 (depth larger than 0.30 m in this particular case).

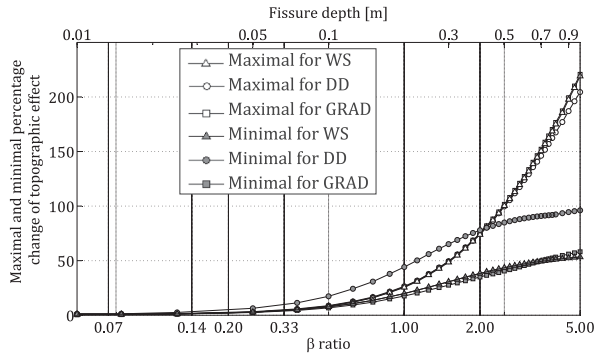

Figure B3. Maximal and minimal percentage change of topographic effect in the pseudo-section, compared to an homogeneous half-space for different fissure depths and for a constant width of 0.20 m, for the WS, DD and GRAD arrays.

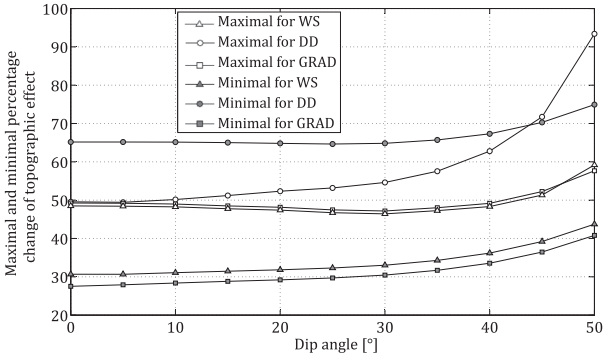

Figure B5. Maximal and minimal percentage change of topographic effect in the pseudo-section compared to an homogeneous half-space, for different fissure dip angles of the reference fissure computed for the WS, DD and GRAD arrays.

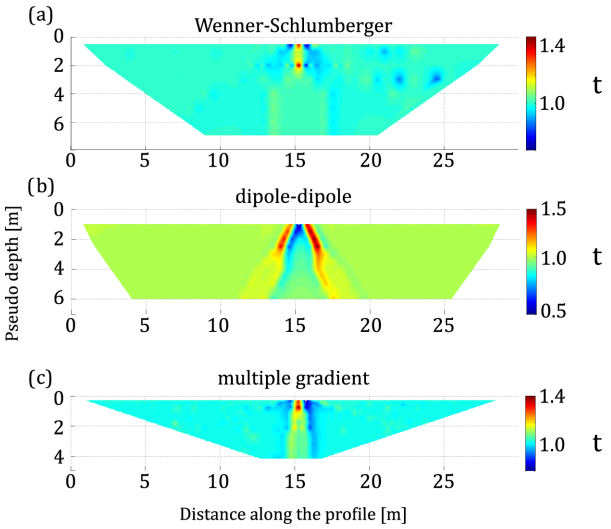

Figure B4. Pseudo-section of topographic effect (t) due to the reference fissure with a dip angle of 30° computed for the (a) WS, (b) DD and (c) GRAD arrays.

B2.3 Effect of fissure dip angle

The dip angle γ (Fig. 4b) effect is tested on the reference fissure, characterized by a depth of 0.30 m and a width of 0.20 m. The dip angle γ ranges between 0° and 50° and the dip is oriented towards the right. The dip angle creates an asymmetry in the topographic effect. This asymmetry is only visible in the topographic effect amplitude but its geometry is unchanged. This phenomena is more visible in the DD and GRAD array pseudo-section presented in Fig. B4. Globally, the maximal and minimal topographic anomaly amplitudes are not affected for dip angles lower than 35° (Fig. B5).

The numerical experiment performed on a reference fissure with a canonical geometry shows that fissure depth and position are the major parameters affecting the topographic effect, and therefore the apparent resistivity. Fissure width and dip angle have less importance (at least for the range of tested parameter values) on the topographic effect anomaly amplitude. These results demonstrate the necessity to measure accurately in the field the fissure depth and location for all fissures deeper than 0.1 times the inter-electrode spacing. The fissure width and dip angle can be measured with less precision.

B3 Effect of the fissure filling

A fissure is a dynamic structure, that can be clogged or opened by a stress change in the media or fully or partially filled with soil or water (Krzeminska *et al.* 2011; Dinka 2012; Stumpf *et al.* 2013). This feature creates an important effect of the fissure on water, gas and nutriment transports by changing the dynamics of preferential water flows (Krzeminska *et al.* 2011; Greve *et al.* 2012). We analyze the effect of the fissure water filling on the apparent resistivity pseudo-sections.

We identify two different possible processes that may impact the raw apparent resistivity pseudo-section calculated using the relation 1.

(i) The partial filling of the fissure by water, that decreases the topographic effect.

(ii) The possible high conductivity of the water, that causes a decrease of apparent resistivity.

To understand these effects, the importance of each process is assessed by numerical modelling. Once again, the reference fissure is used on the same acquisition geometry (0.50 m inter-electrode spacing). The mesh used is presented in Fig. B6.

B3.1 Effect of water in the fissure

Fissure filling by water can largely change apparent resistivity. The first factor of change deals with the change of topographic effect during the fissure filling by water. Indeed, the progressive 'spackling' of fissure decreases the topographic effect and finally make it completely disappear when the fissure is totally filled (f_w equals to 100 per cent). The reference model used is presented in Fig. B6. The soil (red) resistivity is considered as homogeneous. The filling water (blue) is in the fissure. In a first time, the resistivity of both materials is not defined, and only the topographic effect, due to the change of geometrical factor is studied. The filling level of the fissure is defined as the water level compared to the fissure depth. Thus, a filling level of 50 per cent means a water level equal to half its depth. The result is presented as a pseudo-section of percentage change of topographic effect. Thereby, it is comparable to a pseudo-section of percentage change of apparent resistivity acquired with the same configuration at two different dates. The purpose of the study is not to verify that the total filling of the fissure totally suppresses the topographic effect, but to study the dynamic effect of the process of

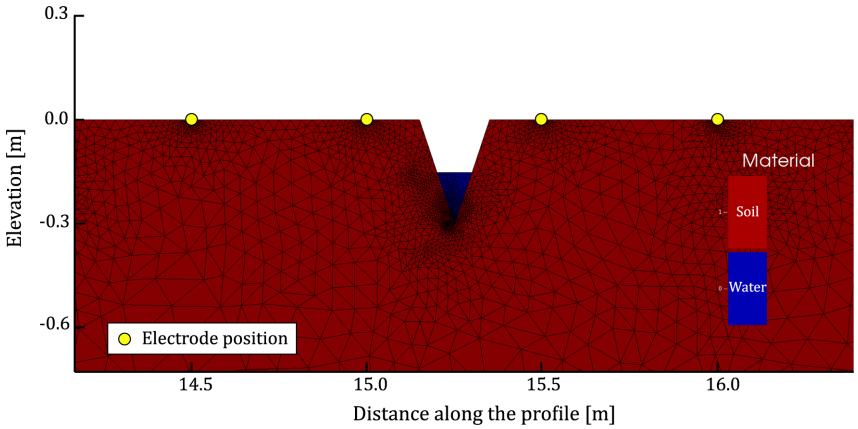

Figure B6. Close-up view of the model used for simulating the water filling in the fissure (example of a water filling of 50 per cent).

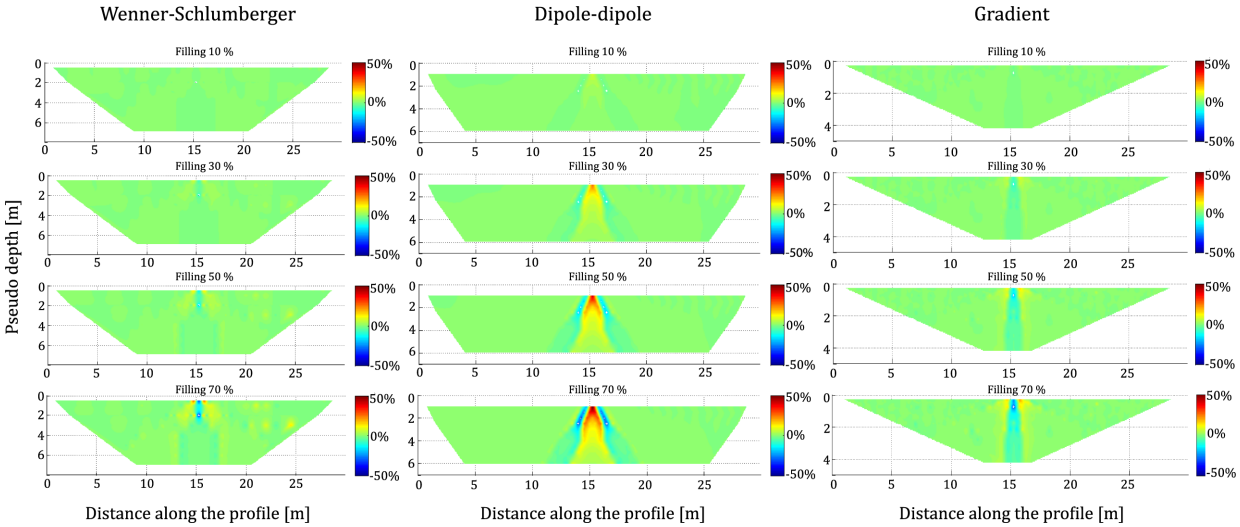

Figure B7. Effect of the water filling of the reference fissure: percentage change of the topographic effect (t) compared to a dry fissure ($f_w = 0$ per cent) computed for the WS, DD and GRAD arrays and for different water filling f_w (a) 10 per cent; (b) 30 per cent; (c) 50 per cent; (d) 70 per cent.

water filling on apparent resistivity (linear or non-linear behavior). Therefore, we only represent results for water filling f_w ranging from 10 to 70 per cent on Fig. B7. The percentage change scale varies from −50 to 50 per cent, which is approximately in the range of percentage change of topographic effect due to the presence of the reference fissure.

As expected, the anomaly is the opposite of the topographic effect due to the presence of a fissure (Fig. 6). Contrarily to the previous sensitivity analysis on the fissure shape parameters, the percentage change of topographic effect varies almost linearly with the water filling level f_w for the three resistivity arrays. We observe nevertheless a slightly non-linear behavior for fissure water filling greater than 70 per cent (Fig. B8). If once again, we fix an error threshold of 5 per cent, assuming that apparent resistivity change lower than this value could be due to noise, only the DD array is impacted by a fissure water filling f_w equal to 10 per cent. We can notice that the DD array has a specific response, different from the ones of the GRAD and WS arrays, which are very similar. The experiment demonstrates the importance to consider water filling for interpreting the apparent resistivity values. Consequently, a water filling greater than 10 per cent off the depth of the fissure has to be taken into account in the interpretation.

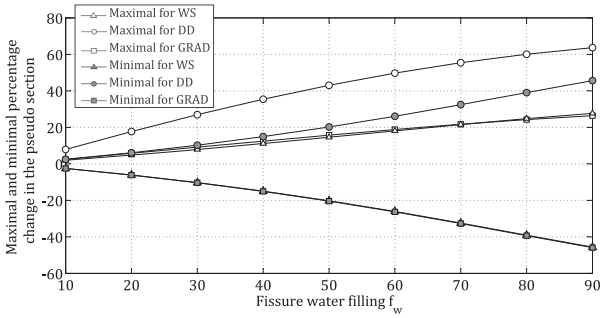

Figure B8. Maximal and minimal percentage change of topographic effect in the pseudo-sections compared to a dry fissure ($f_w = 0$ per cent) for different water filling f_w. The results are presented for the WS, DD and GRAD arrays.

B3.2 Effect of water quality

The presence of water relatively more conductive than the soil could have an impact on the apparent resistivity. Therefore, the pseudo-section of raw apparent resistivity computed with eq. (1) contains both the topographic effect, which multiplies the conductive effect

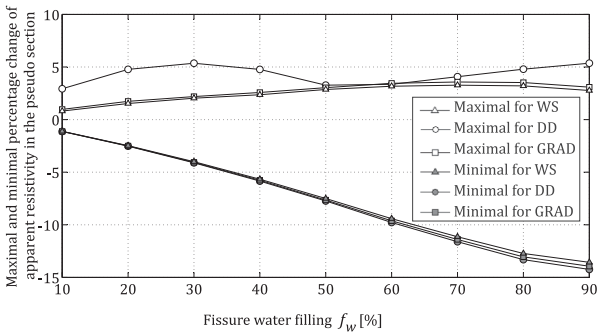

Figure B9. Maximal and minimal percentage change of apparent resistivity in the pseudo-section compared to a dry fissure ($f_w = 0$ per cent) for different water filling f_w values and for a water resistivity equal to 5 Ωm. The results are presented for the WS, DD and GRAD arrays.

of the soil and fissure waters. In this section, we estimate the impact of the conductive effect of the fissure water.

We use the fissure models presented above (reference fissure filled with different fissure water filling f_w). A resistivity of 50 Ωm is affected to the soil. The water resistivity is taken at 5 Ωm. These values are not very important compared to their ratio. The result remains valid for a water resistivity 10 times lower than the soil resistivity. We further compute the percentage change of apparent resistivity compared to a dry fissure ($f_w = 0$), computed with the geometrical factors calculated numerically.

The apparent resistivity pseudo-section anomaly, computed with a geometrical factor calculated numerically, shows a pattern of the topographic effect similar to the one in Fig. B7. As previously, the results are summarized by the maximal and minimal percentage changes in the pseudo-section, compared to a dry fissure, versus the fissure water filling f_w, for the three resistivity arrays (Fig. B9). In this figure, we observe the combined result of the topographic effect change and of the water conductivity effect.

If we compare, the results obtained Fig. B8 and Fig. B9, we can observe that the presence of a conductive water attenuates the variation of the topographic effect compared to a water taken at 50 Ωm, globally resulting in a smaller change on the apparent resistivity.

The results show almost identical responses for the WS and GRAD array and a larger effect for the DD array; they confirm that the water filling f_w parameter can be set to 0 per cent, if the fissure is completely dry or lowly filled at its bottom (f_w lower than 10 per cent). The topographic effect is however too large to ignore water filling greater than 10 per cent.